RESEARCH PAPER

Laser welding of additively manufactured AlSi10Mg and conventionally manufactured Al6061 alloy

A. K. Vishwakarma[1,2] · D. Debnath[1,2] · M. D. Pawar[1] · V. Muthiyan[3] · B. Gautam[4] · R. Khatirkar[5] · Himanshu Shekhar[2] · V. D. Hiwarkar[1]

Abstract

In the present study, laser welding of additively manufactured AlSi10Mg was undertaken with AlSi10Mg (similar) and Al6061 (dissimilar) alloy. The aim was to understand the laser weldability of selective laser melting (SLM)-printed AlSi10Mg alloy without filler material. The similar and dissimilar type of butt joints were prepared, and it is found that dissimilar weldments had better mechanical properties than similar weldments. The heat treatment on these welded plates also improved their mechanical properties. The precipitation of Mg_2Si particles was evident from the XRD and TEM analysis. The as-built cellular structure was broken due to heat treatment and also near the weld zone in the as-welded plate. It was observed that microhardness increased with increase in Mg_2Si content after the heat treatment process. The strength of welded samples was less than that of the base metals. The heat treatment results in ~20% increase in the tensile strength of the welded samples with significant increase in elongation.

1 Introduction

Metal additive manufacturing (MAM) has gained a lot of interest in the recent past owing to its design freedom [1]. Selective laser melting (SLM)/powder bed fusion-based MAM technology has demonstrated successfully with various materials [2, 3]. Military engineering demands light weight parts with complex shapes, internal cavities, etc. Materials such as aluminium alloys and design optimization/simulation techniques [4, 5] are common. Reduced material wastage, reduced cost, on-site and on-demand production,

local tailor-ability, and reduced need for skilled workforce [6] are advantages of MAM that remain unmatched. MAM also offers possibilities of reducing lead times and quick delivery of parts for operations, maintenance, repairs, and overhaul [7].

Aluminium–silicon alloys possess excellent properties such as good corrosion resistance, sound castability, and weldability. Al-Si alloys have been used in various applications particularly in the automotive sector and aerospace industries because of their attractive mechanical properties, high heat conductivity, and low weight [8]. Adding alloying elements like magnesium to the Al-Si alloy enhances mechanical strength after ageing. These precipitates strengthen the matrix to a significant extent without compromising the other mechanical properties. AlSi10Mg alloy contains Mg and can be strengthened through precipitation strengthening mechanism by applying suitable ageing treatment [9]. Furthermore, it is easy to process by laser applications due to the near-eutectic composition of Al & Si which is known to lead to a small solidification range, compared to high strength aluminium alloys (7XXX) series. [2, 8]

Metal additive manufacturing has now been developed as the widely used manufacturing process in the industry for producing highly complex parts [10]. Although MAM

✉ V. D. Hiwarkar
vijayhiwarkar@gmail.com

1   Department of Metallurgical and Materials Engineering, DIAT(DU), Ministry of Defence, Girinagar, Pune, India

2   HEMRL, DRDO, Pune, India

3   COEP Technological University, Pune 411005, Maharashtra, India

4   R&DE(E), DRDO, Pune, India

5   VNIT Nagpur, Maharashtra, Pune, India

has overcome several limitations for engineers, it also brings along a series of challenges. Build size limitation [1, 5, 11, 12] being the key problem can be effectively solved by building smaller parts and welding them together. However, the choice of aluminium alloys as light weight building material poses challenges in welding, such as pore formation and cracking due to its inherent properties [13, 14]. A variety of parts made by MAM using steel [11], AISI 316 [3, 4], Titanium [15], and even dissimilar combinations [16] have been welded together, and their weldability aspects have been explored. Owing to the wide range of applications of additively manufactured AlSi10Mg, the study of its welding to other conventional aluminium alloys needs to be given attention. This welding process will open a new range of applications for additively manufactured parts as they can be effectively used in a large assembly of parts [17].

Limited studies on laser welding of similar AlSi10Mg additively manufactured alloy have been carried out [1, 2, 18, 19]. Schwarz et al. [1] have studied laser welding aspects of AM parts under vacuum in order to improve joint strength by minimizing porosities. Ductility in the weld zone was also found to be decreased due to porosities. Makikangas et al. [2] have also carried out preliminary studies on laser welding aspects of AlSi10Mg and formation of porosities leading to poor mechanical strength. Ambient pressure has strong impact on formation of porosities in weld joint as studied by Chen et al. [18], and the porosity ratio decreases with ambient pressure. Biffi et al. [19] have studied metallurgical aspects due to alteration of eutectic silicon network in the weld zone resulting in reduction of hardness. However, these studies do not cover the laser welding aspects of conventional (sheet metal) parts made of Al 6061 alloy with AM parts (AlSi10Mg) and effect of heat treatment on improvement of mechanical properties.

Welding parameter optimisation has been proved to be crucial for obtaining sound weld joints in additively manufactured alloys, often deviating from that of conventional materials. Conventional methods of welding yield coarser microstructure in the weld bead which can be overcome using solid-state methods like friction stir welding, but the latter poses difficulties in joining complex shapes [11]. Gas tungsten arc welding (GTAW) has been explored as a method for welding MAM parts but imposes certain disadvantages like large weld bead, slower speed, larger heat affected zone, and skilled labour requirement [15]. Laser beam welding (LBW) utilizes a focussed energy source and offers the advantage of reduced heat affected zone and minimal deformation [2, 11],

and robotic welding heads can weld the most complex shapes including thin sheets coupled with improved welding speed and productivity [20, 21].

The present work aims at exploring laser weldability of similar parts (SLM produced AlSi10Mg) and dissimilar parts (SLM produced AlSi10Mg to conventionally produced Al 6061). Here, microstructure and mechanical properties of similar and dissimilar welds (additive manufactured (AM) to another AM part and AM to the conventionally manufactured (CM) part have been characterized and compared. The effect of solutionizing and ageing heat treatment on the mechanical properties of the joined part has also been investigated.

2 Materials and experimental methods

To compare the weldability of AM-AM and AM-CM, plates of AlSi10Mg alloy produced by SLM process and conventional Al 6061 plates were used. The chemical composition (in weight %) of AM and CM plates was determined by an optical emission spectrometer (OES) and is given in Table 1.

AM specimens used in this work were manufactured by SLM method in the form of sheets with the dimension 100 (length) $\times$ 100 (width) $\times$ 3 (thickness) mm^3. The parameters used for printing the AM samples are given in Table 2. After printing, the AM samples were stress relieved at 300 °C for 2 h followed by shot blasting at 2 bar pressure using 120 μm aluminium mesh.

Conventionally manufactured (CM) Al 6061 sheet with T6 heat treatment condition was used for the laser welding. Both CM and AM samples were cut into plates of dimension $100 \times 50 \times 3$ mm^3. The specimens were cut using an abrasive cutting machine (Baincut-M Auto,

Table 2 Details of SLM printing parameters for manufacturing of AM samples

Material	AlSi10Mg
Laser power [W]	400
Layer height [mm]	0.03
Laser focus diameter [μm]	100
Scan velocity [m/s]	7
Type of laser	Yb-fibre laser
Machine make	EOS M 400–4

Table 1 Chemical composition (in weight %) of AlSi10Mg and Al6061 alloy

Alloy	Composition in wt. %								
	Si	Mg	Fe	Cu	Mn	Cr	Zn	Ti	Al
AlSi10Mg (AM)	10	0.3	0.55	0.05	0.45	0.15	0.1	0.05	Bal
Al6061(CM)	0.6	1.0	0.7	0.27	0.15	0.2	0.25	0.15	Bal

Table 3 LBW parameters for welding of AM-AM and AM-CM samples

Pressure [bar]	1
Laser power [W]	2700
Welding velocity [mm/s]	24
Inert gas [l/min]	15
Beam oscillation [Hz]	200
Oscillation amplitude [mm]	0.35

make—Chennai Metco) provided with SiC cut off wheel. Excess coolant and slow cutting speed with very small feed rate was used to avoid any structural transformation due to the heat produced during cutting. After cutting the samples in specified dimensions, they were first cleaned by mechanical brushing. The surfaces to be welded were subjected to rough polishing with polishing papers to ensure complete removal of any foreign particle. After cleaning, the specimens were welded by laser beam welding (LBW) process using a fibre laser in standard condition with the welding parameters as given in Table 3. An illustrative diagram of the welded specimen is shown in Fig. 1. While mounting, minimal gap (~ 0.2 mm) was ensured between the two plates. Shielding gas (argon) was used at a flow rate of 15 l/min to avoid oxidation or any other reaction of the metal with the atmosphere. No filler metal was used

during these experiments. A continuous weld bead was observed after welding (Fig. 2a).

To ensure the repeatability of the process, three samples were welded for each condition representing different combinations, viz. AM-AM and AM-CM. All the specimens were cleaned by mechanical brushing after welding. To obtain heat-treated condition, one welded sample of each combination was aged for 2 h at a temperature of 160 °C in an inert atmosphere [18]. The samples were kept in furnace for ageing immediately after welding and cleaning. The samples were then allowed to cool slowly down to room temperature in the furnace. For further characterization, the samples were labelled as given in Table 4. For tensile testing specimens, the samples were cut from these welded specimens (across the weld) as per ASTM E8 (Fig. 2b).

2.1 Characterization

X-ray diffractometer (Bruker, Germany, model—D8 Advanced) was used for the phase identification and for measurement of residual stresses in the weld zone (WZ) of all four welded specimens and to identify the precipitates present in the weld zone. Measurements were done with CuKα radiation ($\lambda = 0.154056$ nm) and standard Bragg–Brentano geometry within 2θ range of 20–100° for recording diffraction patterns. Residual stress measurement was done by using the $\sin^2\psi$ method on the same machine

Fig. 1 Illustrative figure showing welded specimens: **a** AM-CM and **b** AM-AM
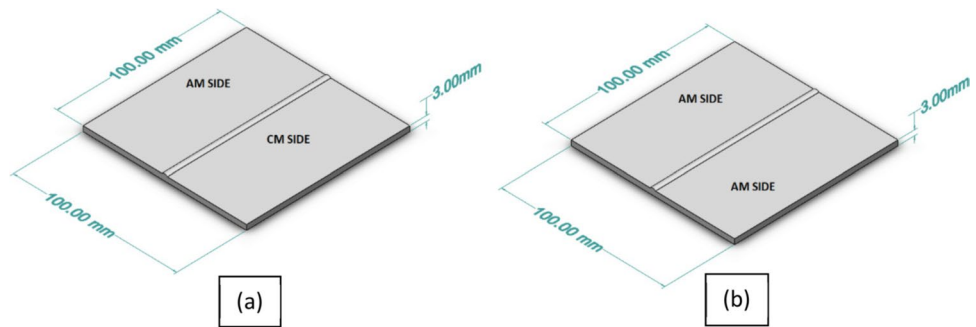
Fig. 2 **a** Actual weld specimen of AlSi10Mg alloy with 100 mm × 100 mm × 3 mm dimension and b tensile test specimen. The tensile specimens were taken from the actual welded samples shown in (**a**)
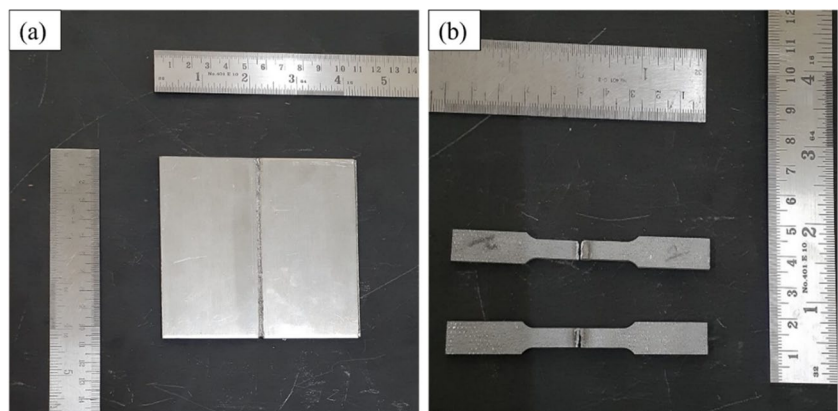
Table 4 Nomenclature for each sample condition

Sr. No	Sample name	Condition
1	AM-AM AW	Both side AlSi10Mg in as-welded condition
2	AM-AM HT	Both side AlSi10Mg with heat-treated condition (after welding)
3	AM-CM AW	AlSi10Mg welded to Al 6061 in as-welded condition
4	AM-CM HT	AlSi10Mg welded to Al 6061 in heat-treated condition (after welding)

[22–27]. Optical microscopy was used to study microstructure at different locations (welded zone, heat affected zone, and base alloy) using Leica, USA, DMi8 optical microscope provided with LASV4.10 image analysis software. Polishing was performed on BAINPOL Chennai Metco, India, polishing machine. Specimens were polished using standard metallographic procedures [28]. The specimens were cold mounted, and polishing was carried out using emery papers from 120 μm grit size to 2500 μm grit followed by final fine polishing on velvet cloth with diamond paste of 3 μm, 1 μm, and 0.25 μm successively. Finally, specimens were cleaned with water and acetone followed by drying using an air dryer. Etching was done with Keller's reagent (2% HF, 6% HNO_3, 92% distilled water, all in volume fractions) for 10 s [8].

The polished and etched samples were observed in a scanning electron microscope. The Zeiss field emission scanning electron microscope with Bruker attachment for EDX (energy-dispersive X-ray spectroscopy) analysis was used. The AM-CM specimens of as-welded and heat-treated conditions were analysed using EDX. The point analysis method was used to determine the change in composition from AM side to CM side. EBSD measurements were done using Quanta 3D FEG SEM with an EDAX EBSD detector with 0.1 μm step size covering an area of 500×500 μm^2 on a plane perpendicular to welding direction. VibroMet machine was used for vibratory polishing to prepare samples for EBSD measurements. Samples were kept for 10 h in the vibromet polishing machine. EBSD parameters, beam, and sample positions were kept identical to avoid any error between the scans. For indexed grains, KAM (the average misorientation of each measurement point with all its neighbours) were estimated considering a tolerance angle of 5°. Thermo Scientific, Themis 300 G3 transmission electron microscopy (TEM) equipped with field emission gun (FEG) operating at 300 keV was used for the TEM studies. The combined super-EDS X-ray detection system with a high current density electron beam in the scanning mode (STEM) was used to observe the precipitates formed. The TEM samples were prepared using standard sample preparation technique.

Hardness measurements were done with microhardness testing machine MMT-X7 (Make: Matsuzawa, Japan). Pyramid-shaped diamond indenter with an included angle of 136° between opposite faces was used. The load was set to 200 gf with a dwell time of 10 s. The hardness measurements were done as per ASTM E-384 standard. Hardness measurements were performed in different regions of the specimen, viz. BM, HAZ, and WZ perpendicular to the weld direction. At least eight measurements were performed in each region. The tensile specimens were tested at room temperature on Hounsfield, universal testing machine (UTM) of capacity 25 kN, keeping the crosshead speed of 0.06 mm/min. Three samples were tested of each combination. Test parameters were kept constant between the samples to have uniformity in the deformation conditions for all the samples.

3 Results and discussion

3.1 XRD analysis

Figure 3 illustrates the XRD patterns of the weld zone of AM-AM and AM-CM laser welds, both in as-welded (AW) and heat-treated (HT) condition. The diffraction peaks of Al (111), (200), (220), Si (311), (220), and Mg_2Si precipitates are shown in Fig. 3 which are in agreement with the peak positions reported in the literature [19, 22]. Significant difference of peak intensities was observed in AW and HT samples. The full width half maximum (FWHM) values and the position of major peaks of Al are shown in Table 5. According to the values listed in Table 5, FWHM analysis shows that there is a peak narrowing, i.e. decrement in peak width after heat treatment. This peak narrowing is also shown in Fig. 3, in as-welded and heat-treated condition.

For AM-AM sample, the FWHM value decreases after heat treatment which indicates that the strain is decreasing, whereas peak shift reduces from the exact peak position, which indicates drop in stress after heat treatment [23–27]. In case of AM-CM samples, the effect of heat treatment on strain is similar to that of AM-AM samples, and here too, the shift of peak position follows the same trend as that of AM-AM samples. It is quite apparent the possibilities of diffusing out Si from the Al matrix during the heat treatment which leads to the improvement in peak intensity of Si as shown in Fig. 3 [9, 21]. Figure 4 shows the residual stresses in welded region of AW and HT samples. Both AM-AM and AM-CM welded samples shows compressive residual stresses with the values of −126.6 MPa and −98.5 MPa, respectively. After heat treatment, the
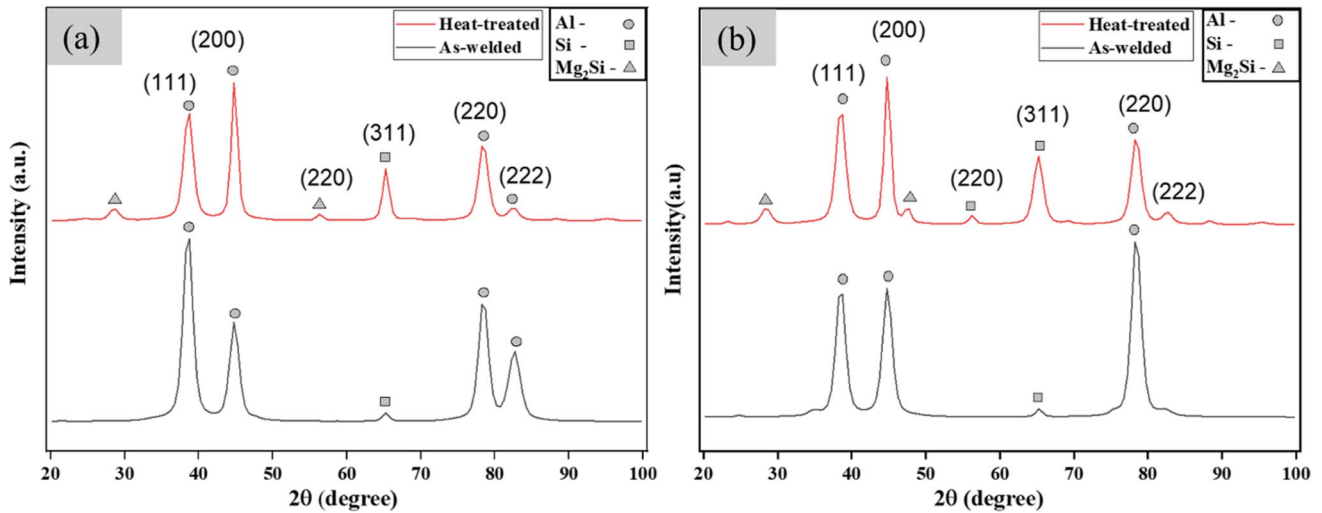
Fig. 3 XRD pattern of **a** AM-AM and **b** AM-CM weld zone in as-welded and heat-treated conditions

Table 5 FWHM values and position of XRD peaks

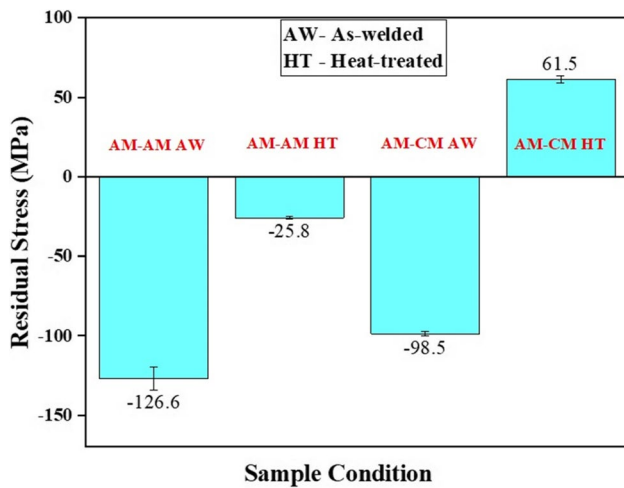| Sample name	FWHM (°)	Position (2θ, °)
AM-AM AW	2.4	78.13
AM-AM HT	1.2	78.34
AM-CM AW	2.4	78.14
AM-CM HT	1.8	78.32

**Fig. 4** Residual stress comparison of AM-AM and AM-CM sample in as-welded and heat-treated conditions

AM-AM sample showed drastic drop in the residual stress (− 24.8 MPa). The drop in the residual stresses after heat treatment was associated with stress relieving operation. In case of AM-CM sample, the heat treatment did not show much drop except the change in compressive to tensile nature (61.5 MPa).

3.2 Microstructure analysis

3.2.1 Microstructure of base metal

Figure 5 shows the optical microstructures of base metals for additive manufactured (AM) AlSi10Mg and conventional manufactured (CM) Al6061 alloy. Figure 5a and c shows the microstructures of base metal samples, whereas Fig. 5b and d shows the microstructures of heat-treated samples of the base metal. AM microstructures show a uniform distribution of silicon all over the matrix of Al. The AlSi10Mg has near-eutectic composition, and the structure shows the mixture of Al and Si. The laser marks are clearly visible in Fig. 5a. The base metal of AM shows fine distribution of silicon which is due to faster solidification rate observed in SLM produced parts. After heat treatment, the morphology of silicon changes from sharp needle-shaped to globular type (Fig. 5b). The CM microstructures have an elongated grain structure typically seen in rolled, forged, or extruded samples, with precipitates of Mg_2Si. After heat treatment, the structure becomes equiaxed with more precipitates of Mg_2Si.

Figure 6 shows the microstructures of as-welded AM-AM sample, AM-AM heat-treated (after welding), as-welded AM-CM, and AM-CM heat-treated (after welding) samples. The transition from weld zone to HAZ to base metal is clearly visible. Though the changes are clearly visible for weld zone and base metal, still distinguishing the HAZ from weld zone to base metal can be possible with approximate measurements. The correct measurement of heat affected zone is appeared to be difficult. Hence, the approximate width of HAZ was marked for all three microstructures. The range of width was found to be between 20 and 50 μm approximately. Figure 6c and d shows all three zones of
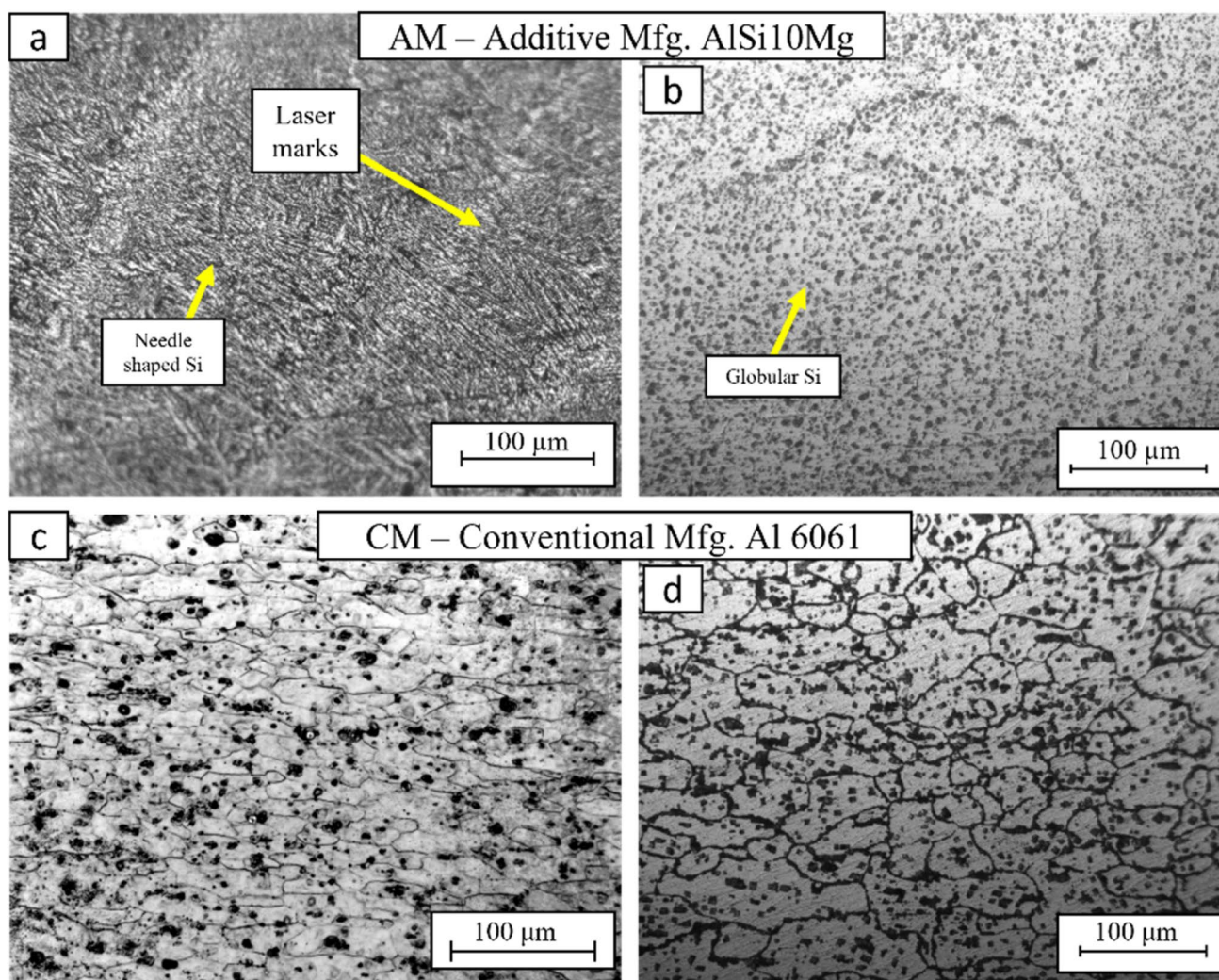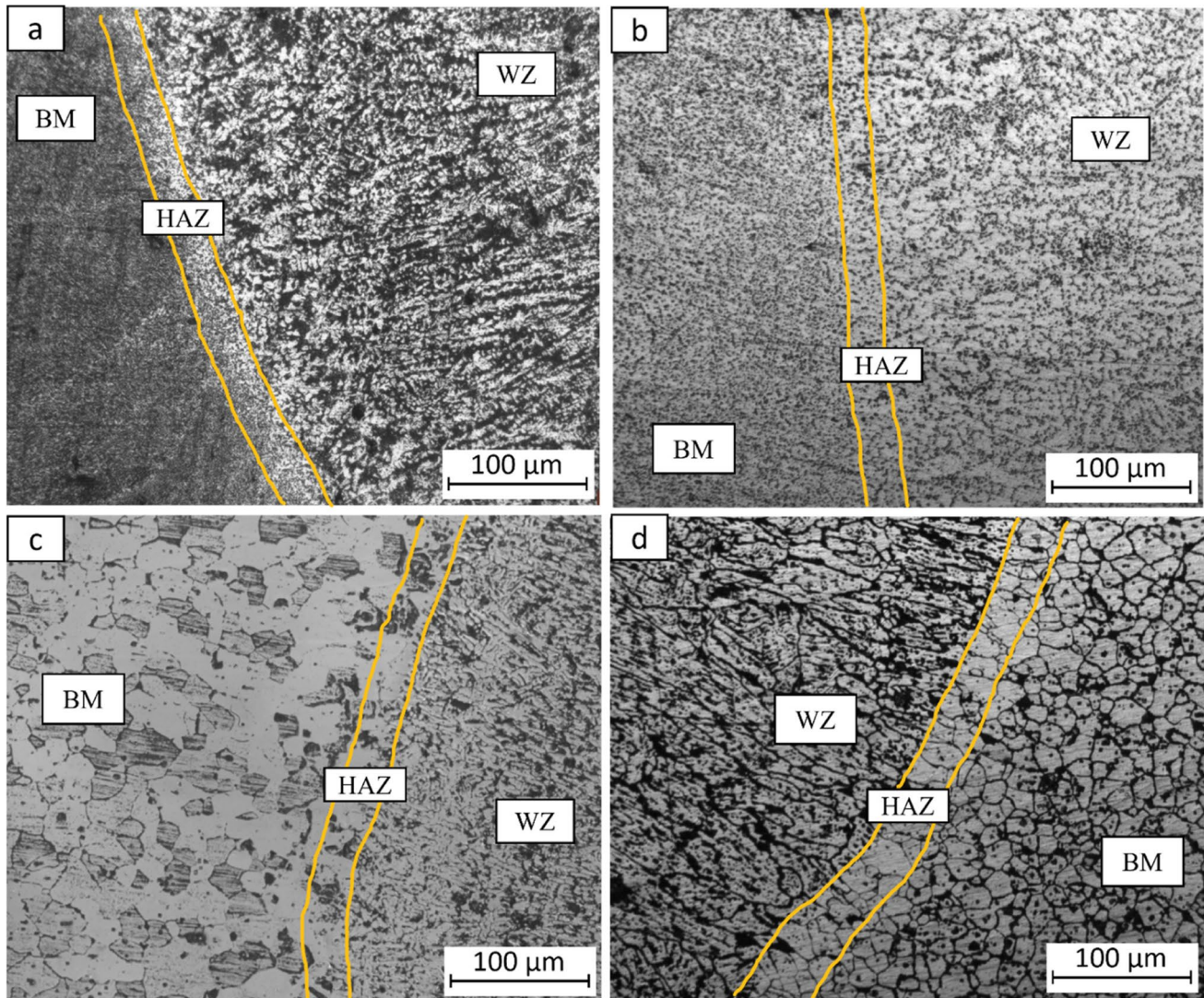
Fig. 5 Optical microstructures of base metals: **a** AM (AlSi10Mg alloy), **b** AM (heat-treated), **c** CM (Al6061 alloy), **d** CM (heat-treated)

AM-CM samples for as-welded and heat-treated condition, respectively. In both the conditions, the difference in the microstructure with dendrites at the weld zone and equiaxed microstructure in HAZ and base Al 6061 alloy is observed. The difference in the microstructure is clearly visible in AM and CM side.

To evaluate further in weld zone, microstructures with higher magnification were taken and shown in Fig. 7. In the weld bead, Al matrix solidifies early due to a high cooling rate, and the excess Si is then driven out of the Al matrix and diffuses along the grain boundaries of α-Al. The microstructure of the weld depends on the gradient in temperature (G) and solidification rate (R) [19, 23]. In laser welding, the solidification time is more than that observed during solidification of metal during SLM printing but still is high enough to avoid the formation of any undesired phases [19]. Therefore, a structure is observed in the weld zone where fibrous type network of silicon is present outside the α-Al

dendrites (Fig. 7a and c). The porosity observed in the weld zone was calculated around 3–5%. The porosity in AM-AM welded region appears to be on higher side as compared with AM-CM welded structure. Immediately after the welding, one set of samples from each weld condition were taken for the heat treatment. After the heat treatment for both welded samples, the silicon redistribution takes place with breaking of fibrous network of Si into finely dispersed Si in the weld zone along with the precipitates. The improvement in Mg_2Si precipitate was due to the high Mg content in the CM base metal and ageing treatment.

After HT, the silicon segregation becomes less and its morphology becomes globular, but still difference in distribution of silicon from HAZ to base metal of AM can be seen (Fig. 8). The size of α-Al decreases from the weld zone towards the base metal of AM side. A similar trend is observed with silicon size as well. The silicon in weld zone is distributed around the initial α-Al region even after

Fig. 6 Optical microstructures showing base metal, HAZ, and weld zone of **a** AM-AM (as-welded), **b** AM-AM (heat-treated), **c** AM-CM (as-welded), and **d** AM-CM (heat-treated) sample. In (**a**) and (**b**), base metal is AM, and in (**c**) and (**d**), base metal is CM

HT. The base metal silicon of AM is much more finely distributed than the weld zone after the HT due to its original morphology. This has been clearly indicated in Fig. 8. The silicon content in AM-CM varies from CM region to AM region. CM side has extremely low Si content (0.4 wt%), whereas the AM side has high Si content (10 wt%). Therefore, the weld zone of AM side and CM side shows different microstructures (Fig. 6). The silicon on the AM base metal, after HT is appeared to be finely distributed all over the matrix. The weld zone on CM side however shows a different morphology. It shows a columnar structure with silicon distributed evenly. During the solidification silicon differs from the AM side (high conc.) towards the CM side (low conc.). The HAZ of CM side shows the start of equiaxed structure with low silicon. The width of HAZ on CM side is very minimal usually observed in laser welding. The

precipitates of Mg_2Si can also be seen in CM structure. The silicon is extremely low on this side and therefore can be barely seen. Figure 6 clearly shows that with the variation of silicon from left to right i.e., from AM to CM, the distribution of silicon is different.

3.2.2 SEM and TEM analysis

Figure 9 displays the SEM images of the weld zone for the AM-AM and AM-CM weld samples captured by secondary electron (SE) detector. Figure 9a shows as-welded structure taken at the centre of the weld, whereas Fig. 9b shows heat-treated structure of AM-AM weld sample and Fig. 9c and d shows the as-welded and heat-treated structure at the centre of AM-CM weld joint.
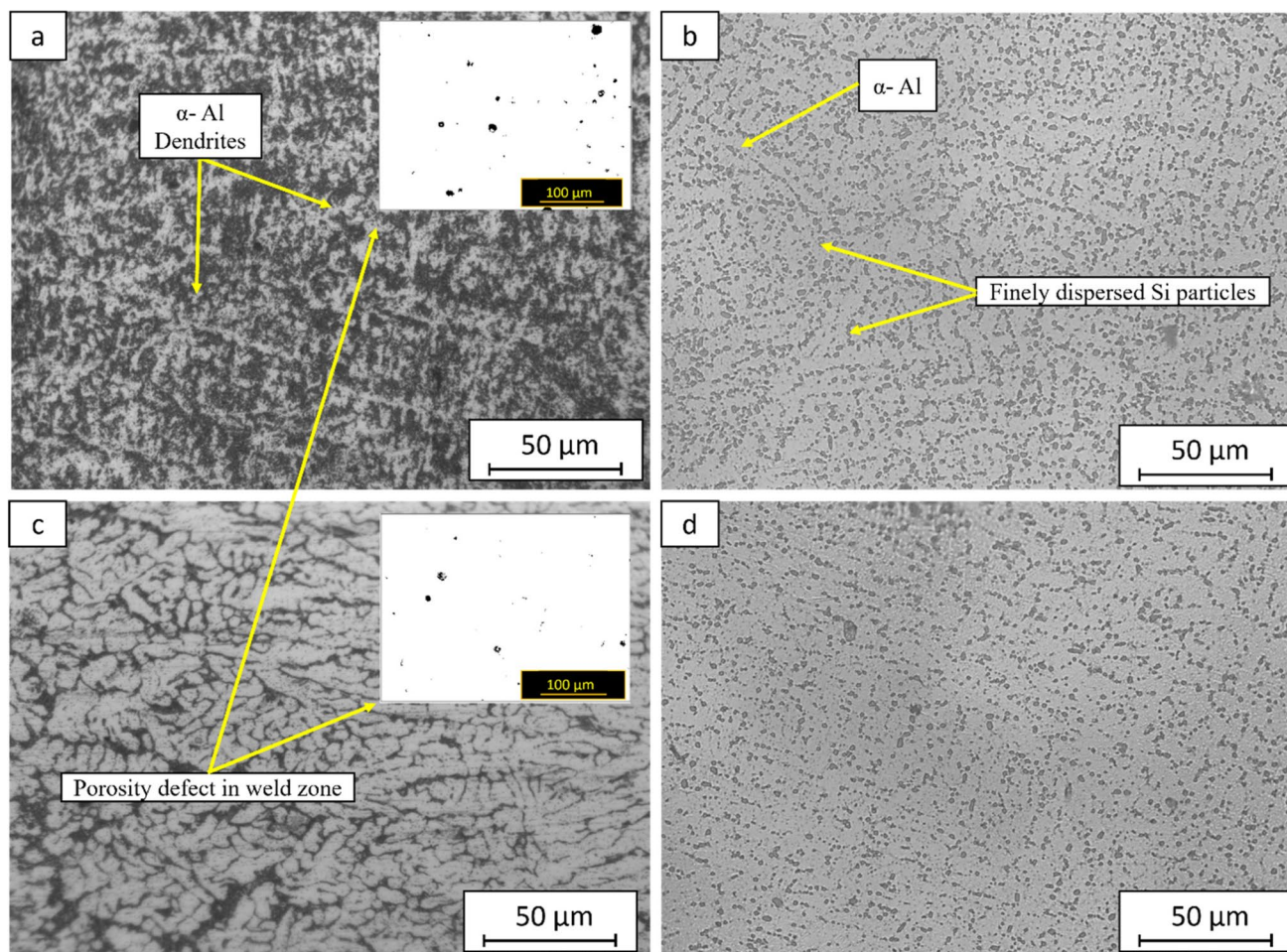
Fig. 7 Microstructures of weld zone for AM-AM and AM-CM samples for **a** as-welded (AM-AM), **b** heat-treated (AM-AM), **c** as-welded (AM-CM), and **d** heat-treated (AM-CM) conditions. Insight in (**a**) and (**c**) images show the porosities in the weld zone

The SEM images clearly show and validate the change in silicon morphology. The Si particles are uniformly dispersed in all areas of the microstructure. The formation of these evenly distributed particles at low temperature is attributed to the diffusion of Si from the oversaturated primary Al matrix. The cellular network of Si starts to collapse and break into equiaxed particles, and the density of particles within the Al grains decreases. Also, during the welding of the plates, due to concentration and thermal gradient developed, the weld experiences the Marangoni convection effect in the molten material, i.e. in the weld zone. This effect causes intermixing of the alloying elements from the base metals [23].

The chemical composition of the as-welded and the heat-treated samples (AM-CM (AW) and AM-CM (HT)) were analysed using EDS detector. The graphs in Fig. 10a and b show the variation in chemical composition from CM to AM side in as-welded and heat-treated samples, respectively. It is observed that the weld zone composition varies from the base metals of both the alloys to the weld zone. The chemical composition graph demonstrates how, in the weld zone, the silicon concentration gradually drops from the AM side to the CM side, and Mg content gradually increases from the AM to the CM side. The Si content drops from around 10 wt% on AM side to 0.3 wt% on CM side, and the Mg content drops from 1.0 wt% on CM side to 0.3 wt% on AM side.

To understand further, the presence of precipitates in weld zone for both AM-AM and AM-CM joints after heat treatment, and TEM analyses were carried out. Figure 11 shows the STEM-BF images with EDS analysis. A clear signature of Mg_2Si precipitates is observed in the microstructures. This is further confirmed with EDS maps (Fig. 11c) where the maps of Si and Mg elements are observed. A needle shape morphology is observed in the matrix of α-Al in AM-AM and AM-CM welded joint after heat treatment. Similar morphology of Mg_2Si precipitates has been shown by Amir et al. [29].
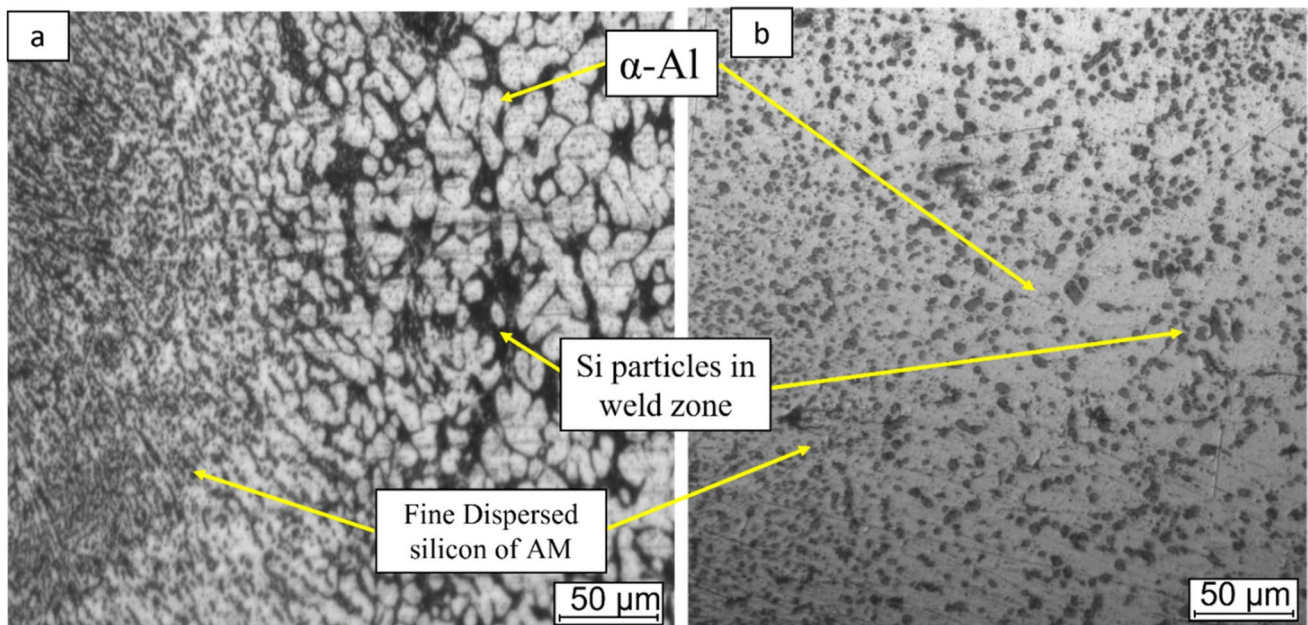
Fig. 8 Microstructures of HAZ showing AM side of AM-CM samples for **a** as-welded and **b** heat-treated conditions with variation in Si size and morphology

3.2.3 EBSD analysis

Figure 12 and Fig. 13 show the inverse pole figure (IPF) maps of welded and heat-treated samples. In Figs. 12 and 13, the overall orientation of the grains appears to be random. The IPF maps show the clear understanding of orientations and grain morphology of the processed samples. Figure 12a shows IPF map of AM base AlSi10Mg alloy having the morphology of additively manufactured sample with melt pool boundaries. Majority of the grains are columnar along with little amount of equiaxed structure is observed. The equiaxed grains mostly featured at the melt pool boundaries, where partial melting of the previously deposited layer occurred during melting of the successive powder layer. After heat treatment, the additively manufactured microstructure completely disappeared (Fig. 12b). The CM base metal IPF map in Fig. 12c shows an equiaxed annealed structure usually observed in Al6061 alloy. Figure 12d shows the heat-treated structure of Al6061 alloy with increased grain size. The grain growth occurs due to temperature given to the material which is more than recrystallization temperature.

Figure 13 shows the IPF maps of the welded zone of AM-AM samples and AM-CM samples both in as-welded and heat-treated conditions. In as-weld condition for both AM-AM and AM-CM samples, the weld pool shows the coarse and dendritic structure usually observed in cast alloys. After heat treatment for both the conditions, the observed change in microstructures shows slight refinement. Figure 14 gives the kernel average misorientation (KAM) maps in the base metals and weld zones both in as-weld and heat-treated conditions of AM-AM and AM-CM samples. KAM values obtained from EBSD data can be used to analyse stress concentration, since KAM has a similar distribution with stress, as illustrated by Ramazani et al. [22]. The misorientation in terms of KAM values are plotted in graphical form. The blue line corresponds misorientation in as-welded condition, while red line represents misorientation in heat-treated condition. The misorientations in case of heat-treated samples are observed to be lower than that of as-welded samples.

3.3 Microhardness

The microhardness was measured using micro-Vickers hardness tester with a load of 200 gf and dwell time of 10 s. Figure 15a and b represents the obtained microhardness profiles for AM-AM and AM-CM samples. The hardness varies from the base metal to the weld zone which is clear in the Fig. 15. The hardness of weld zone region in AM-AM is lower than the base metal of AM. This is due to the coarse cast like structure observed in the weld zone where silicon is present in the fibrous network outside the α-Al dendrites, which gives it a comparatively lower hardness value. The defects like porosity and inhomogeneity may also contribute to lower hardness value of weld zone [21]. The silicon in AM base metal side is finely distributed and thus yields higher microhardness of base metal than the weld zone. The hardness of HAZ of AM sample shows slight enhancement.
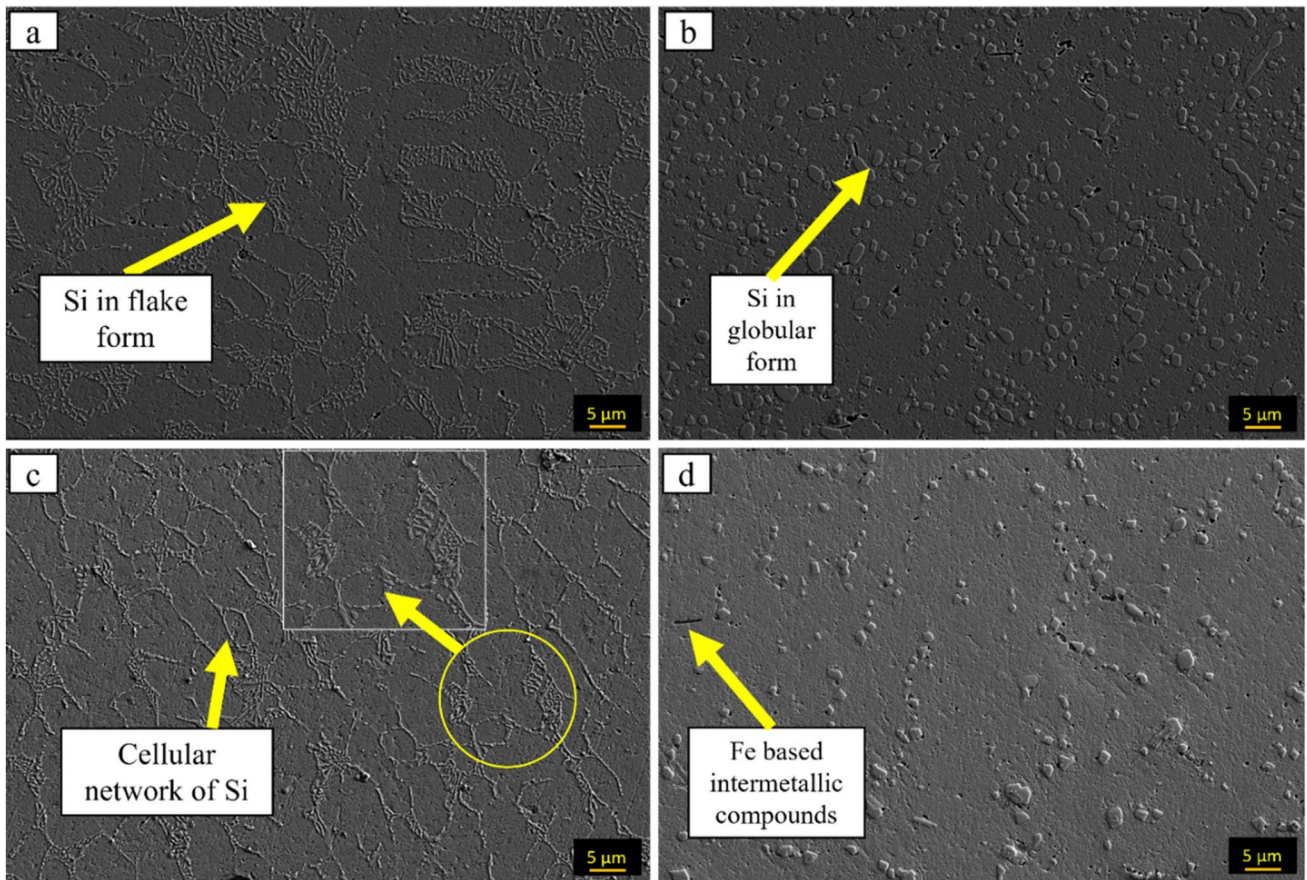
Fig. 9 FESEM micrographs of weld zone of **a** AM-AM (as-welded), **b** AM-AM (heat-treated), **c** AM-CM (as-welded), and **d** AM-CM (heat-treated) samples. The FESEM micrographs are taken in the secondary electron (SE) imaging mode. Insight in (**c**) shows the enlarge view of silicon network
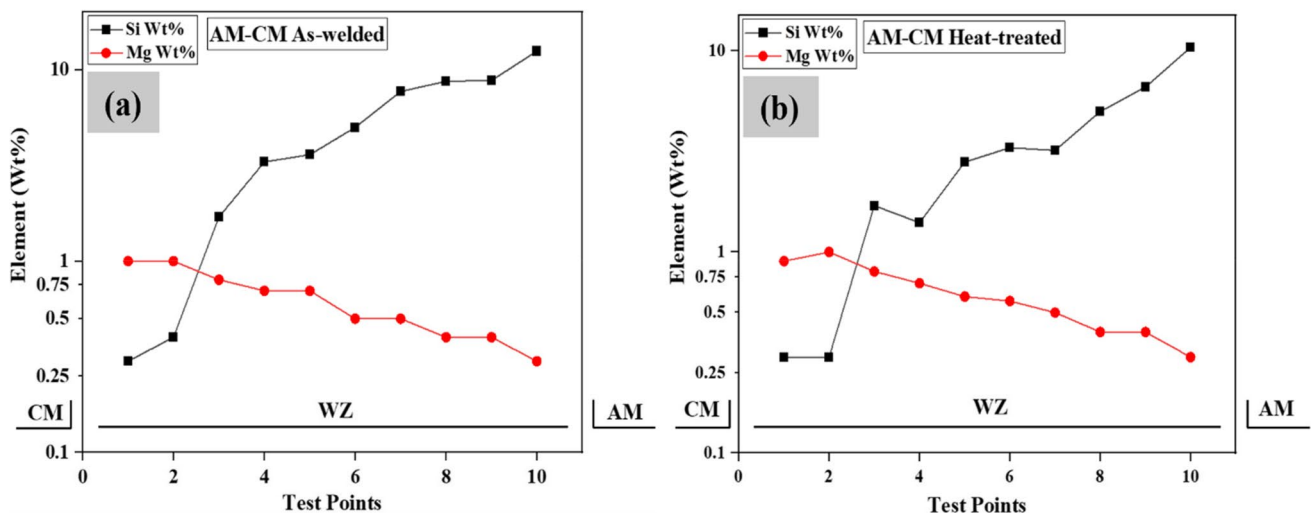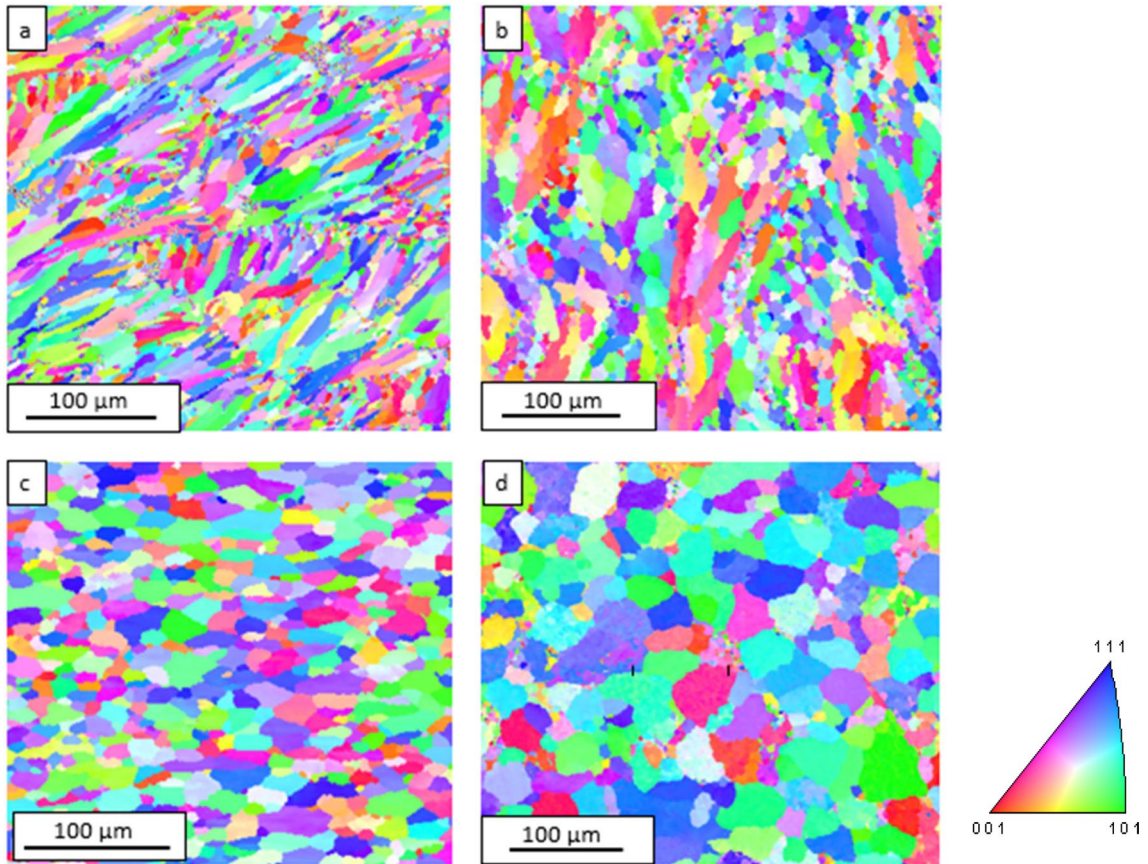

Fig. 10 Compositional variation of Si and Mg elements (in log scale) in the weld zone of **a** AM-CM (as-welded) and **b** AM-CM (heat-treated) samples
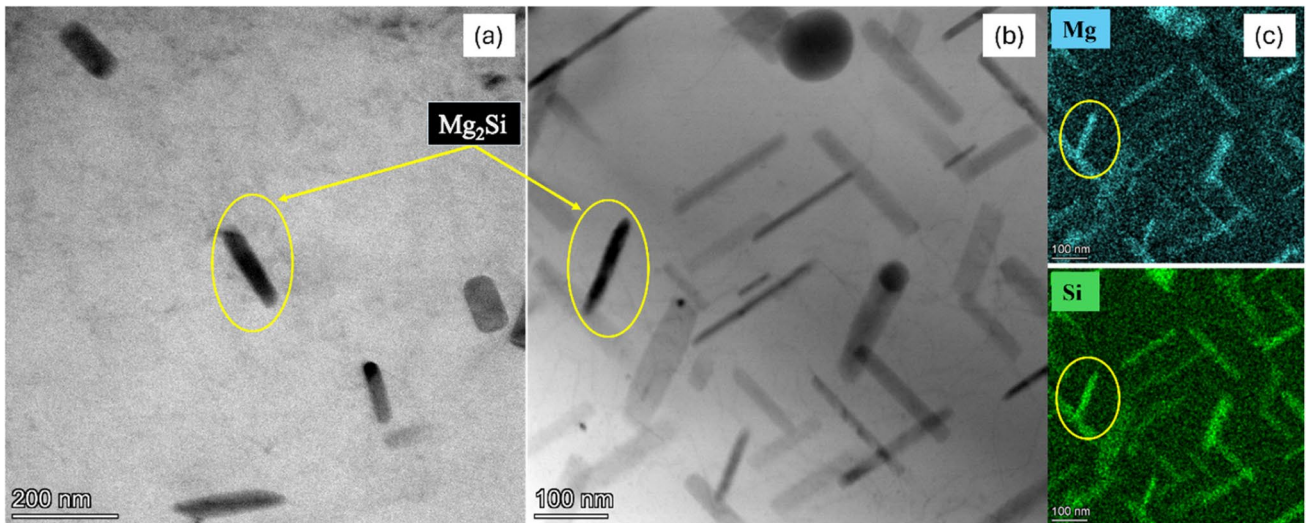
Fig. 11 STEM-BF images of heat-treated **a** AM-AM and **b** AM-CM weld zone, showing the presence of Mg_2Si precipitates and **c** corresponding Mg and Si, EDS elemental maps of AM-CM sample

Fig. 12 Inverse pole figure images of **a** AM (base metal), **b** heat-treated AM (base metal), **c** CM (base metal), **d** heat-treated CM (base metal) sample
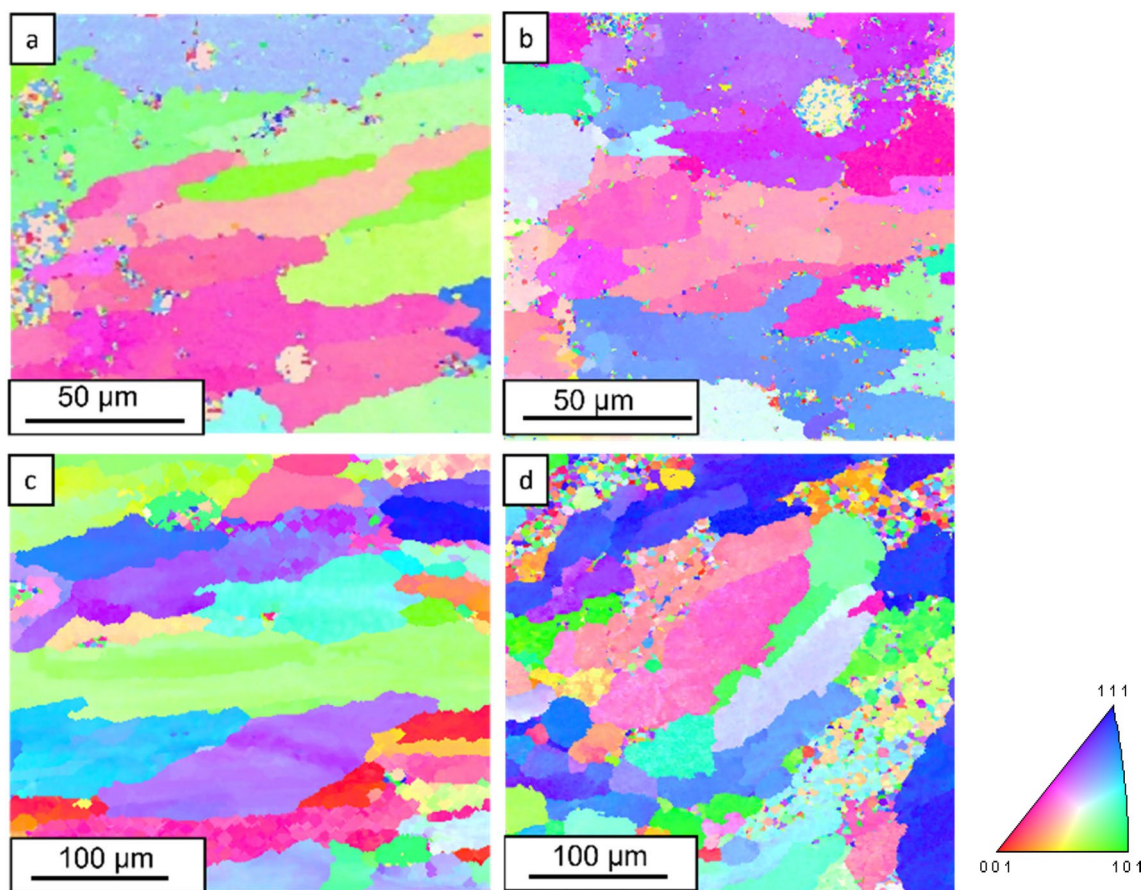
Fig. 13 Inverse pole figure images of weld zones in **a** AM-AM (as-welded), **b** AM-AM (heat-treated), **c** AM-CM (as-welded), **d** AM-CM (heat-treated) samples

This change is attributed to refinement of grain size in heat affected zone. After heat treatment (HT), the redistribution and breaking of silicon particles takes place; this increases the overall hardness of the specimen in all three regions [15]. Also, after heat treatment, the formation of little amount of Mg_2Si contributes in enhancement of overall hardness in AM-AM sample. The presence of intermetallic compounds like Al_5FeSi cannot be ignored as it also contributes in enhancement of hardness [15].

Figure 15b shows the microhardness profile before and after heat treatment of AM-CM samples. The similar trend of increase in hardness from weld zone to base metal is seen before heat treatment. The hardness of the CM base sample shows higher hardness than the AM base sample. This is due to the difference in silicon morphology, i.e. change from fibrous network to the finely distributed globular particles of silicon in the specimen and chemical composition of both the alloys. The HAZ and weld zone of as-welded sample does not show much change in hardness value (Fig. 15b). The weld zone hardness after HT increases due to the complete change in morphology of silicon and increase in the Mg content as evident in

Fig. 9 and Fig. 10. This leads to formation of Mg_2Si precipitates which contributes in increase in hardness of weld zone. The hardness may also increase due to the diffusion of silicon from high concentration side to low concentration side. The hardness of HAZ and BM-CM shows good hardness because of the formation Mg_2Si precipitates.

It is also observed that the weld zone of the dissimilar metals shows greater hardness than the weld zone of similar metal. This is due to the mixed composition observed in the weld zone which will aid in more precipitation of Mg_2Si precipitates.

4 Tensile test

Tensile test results are shown in Fig. 16. Comparison of ultimate tensile strength and % elongation is made in as-weld and heat-treated condition for AM-AM and AM-CM weld samples. In all the samples, the effect of heat treatment is showing the enhancement in tensile properties. Tensile strength and elongation have improved
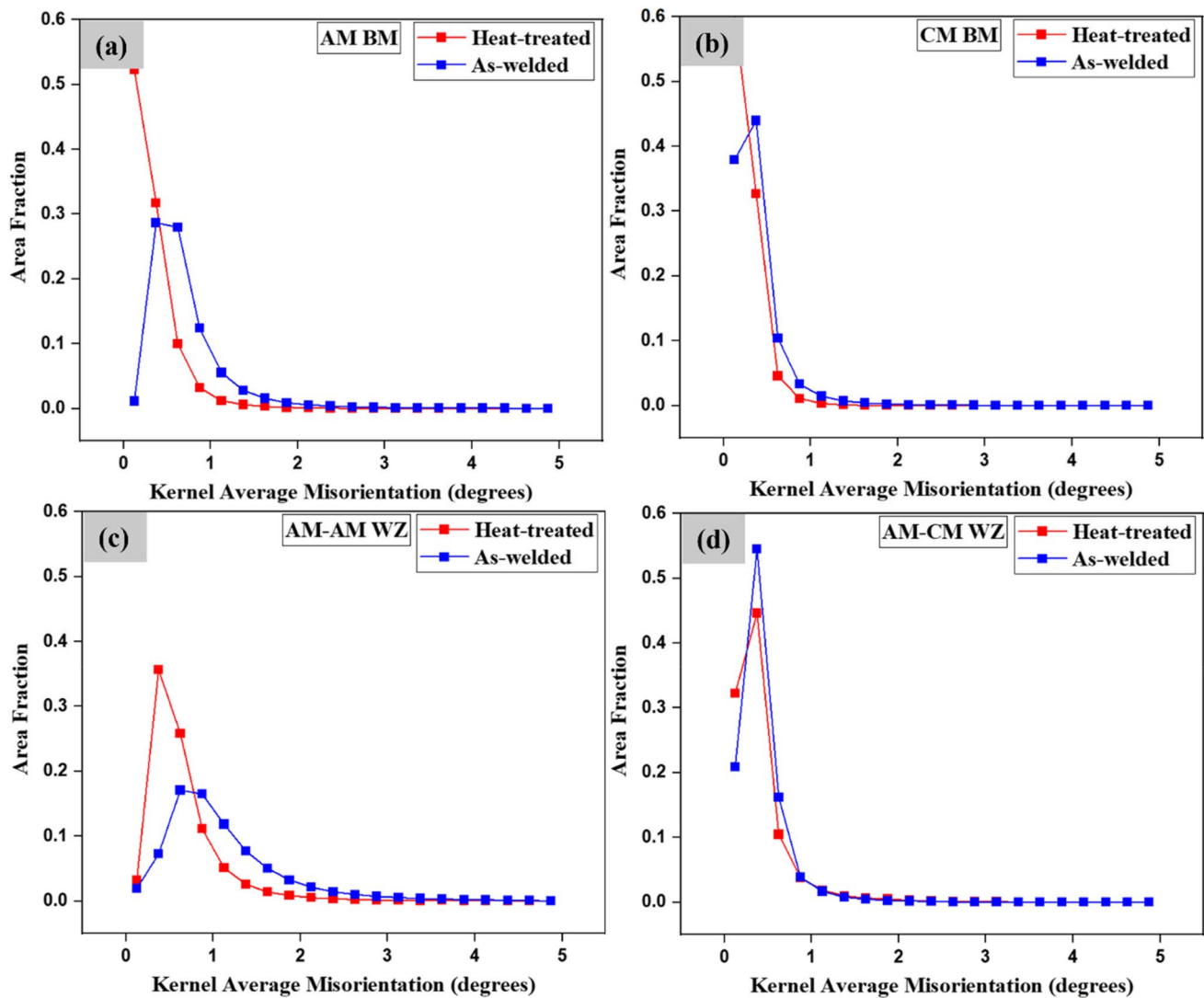
Fig. 14 Kernal average misorientation of **a** AM (base metal), **b** CM (base metal), **c** AM-AM (weld zone), **d** AM-CM (weld zone), for as-welded and heat-treated conditions

after heat treatment. The UTS for AM-AM sample before heat treatment is 119.15 MPa which considerably increased by nearly 20% followed by similar increase of elongation. For AM-CM sample, the increase in UTS is observed to be about 22%. The development of the tensile properties is in line with the hardness values. The uniform distribution of Si particles in the weld zone along with some precipitates like Mg_2Si accounts for this increase of tensile strength in all the samples. Failure of all the samples takes place at weld zone showing lower strength. This failure of material exactly at the weld centre can be seen as shown in Fig. 2b. Failure in these cases was flat fractures on the fracture surface. The flat fracture implied that the microstructure experienced less deformation before fracture. The enhancement in percentage elongation was measured to be 0.58% for AM-AM weld and 1.89% in AM-CM weld samples. The complete tensile test results of base metal are given in Table 6. Ultimate tensile strength of CM base metal sample is more than double to that of the AM base metal, whereas there is no large difference of elongation between these two materials. The prior was associated with the preheating of AM sample 300 °C for 2 h followed by shot blasting.

5 Conclusion

The laser weldability of similar and dissimilar aluminium alloys manufactured using AM and CM samples has been examined in the current work. Additionally, the effect of heat treatment on the same has been studied.
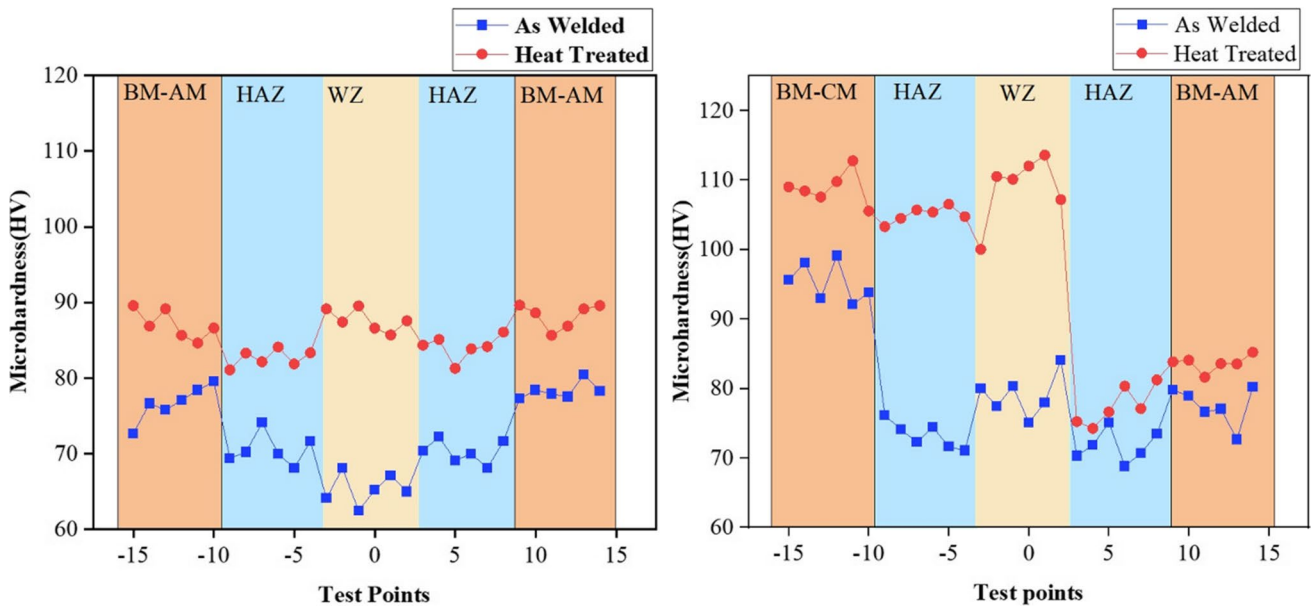
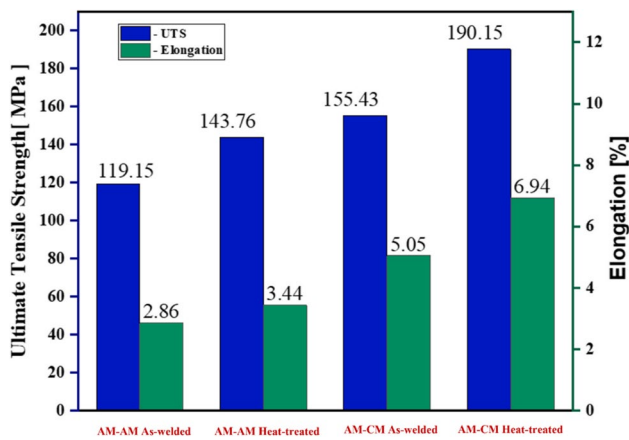**Fig. 15** Microhardness comparison of **a** AM-AM and **b** AM-CM, in as-welded and heat-treated condition

Fig. 16 Tensile properties of AM-AM and AM-CM welded samples both in as-welded and heat-treated condition

- It is possible to weld conventional Al 6061 and additively manufactured AlSi10Mg parts using laser welding process.
- The EDX analysis revealed the clear modification of weld zone in terms of Si and Mg content in dissimilar welding of additively manufactured (AM) and Al6061 samples. Silicon content gradually increased from CM to AM side through the weld zone and the Mg content decreased from CM to AM side due to the Marangoni effect. The effect of heat treatment on these variations in compositions was minimal.
- Enhancement of ultimate tensile strength for both similar and dissimilar welded samples after the heat treatment was recorded around 20–22%. Similarly, a significant improvement was also observed in the elongation.
- The hardness of the weld zone in dissimilar welded (AM-CM) sample increased after the heat treatment. The enhancement in the hardness was attributed to enhancement of Mg content in the weld zone and formation of Mg_2Si precipitates.

Declarations

Conflict of interest The authors declare no competing interests.

Table 6 Tensile properties of AlSi10Mg and Al6061 alloys in as-received condition

Sample name	Stress (MPa)	Elongation (%)
AlSi10Mg (AM) alloy	212.31	15
Al6061 (CM) alloy	272.8	17

References

1. Schwarz A, Schleser M, Gerhards B, Popoola P, Gebhardt A (2021) Welding of additive manufactured Alsi10mg: using laser welding in a vacuum for high quality weld seams — a new approach to welding LPBF manufactured AlSi10Mg. S Afr J Ind Eng 32(4):99–112. https://doi.org/10.7166/32-4-2513

2. Mäkikangas J, Rautio T, Mustakangas A, Mäntyjärvi K (2019) Laser welding of AlSi10Mg aluminium-based alloy produced by selective laser melting (SLM). Procedia Manuf 36:88–94. https://doi.org/10.1016/j.promfg.2019.08.013

3. Matilainen VP, Pekkarinen J, Salminen A (2016) Weldability of additive manufactured stainless steel. Phys Procedia 83:808–817. https://doi.org/10.1016/j.phpro.2016.08.083

4. Mokhtari M, Pommier P, Balcaen Y, Alexis J (2021) Laser welding of aisi 316l stainless steel produced by additive manufacturing or by conventional processes. J Manuf Mater Process 5(4):136. https://doi.org/10.3390/jmmp5040136

5. Emmelmann C, Beckmann F (2015) Hybrid lightweight design by laser additive manufacturing and laser welding processes. Lasers in Manufacturing Conference 2015. Munich

6. Munro C (2019) Review of Structural additive manufacturing for defence applications current state of the art. Defence research and development Canada scientific report, DRDC-RDDC-2018-R212

7. den Boer J, Lambrechts W, Krikke H (2020) Additive manufacturing in military and humanitarian missions: advantages and challenges in the spare parts supply chain. J Clean Prod 257:120301. https://doi.org/10.1016/j.jclepro.2020.120301

8. Louvis E, Fox P, Sutcliffe CJ (2011) Selective laser melting of aluminium components. J Mater Process Technol 211(2):275–284. https://doi.org/10.1016/j.jmatprotec.2010.09.019

9. Kempen K, Thijs L, Van Humbeeck J, Kruth JP (2012) Mechanical properties of AlSi10Mg produced by selective laser melting. Phys Procedia 39:439–446. https://doi.org/10.1016/j.phpro.2012.10.059

10. Kempen K, Thijs L, Van Humbeeck J, Kruth J-P (2015) Processing AlSi10Mg by selective laser melting: parameter optimisation and material characterisation. Mater Sci Technol 31(8):917–923. https://doi.org/10.1179/1743284714Y.0000000702

11. Caiazzo F, Alfieri V (2021) Optimization of laser beam welding of steel parts made by addit manuf. Int Journ of Adv Manuf Tech, 114:3123–3136. https://doi.org/10.1007/s00170-021-07039-w/Published

12. Aboulkhair NT, Simonelli M, Parry L, Ashcroft I, Tuck C, Hague R (2019) 3D printing of aluminium alloys: additive manufacturing of aluminium alloys using selective laser melting. Prog Mater Sci 106:100578. https://doi.org/10.1016/j.pmatsci.2019.100578

13. Kutsuna M, Kitamura S, Shibata K, Sakamoto H, Tsushima K (2006) Tsushima Improvement of the joint performance in laser welding of aluminium alloys. Weld World 50:22–27

14. Pinto LA, Quintino L, Miranda RM, Carr P (2010) Laser welding of dissimilar aluminium alloys with filler materials. Weld World 54:R333–R341

15. Zhang C et al (2019) A comparison between laser and TIG welding of selective laser melted AlSi10Mg. Opt Laser Technol 120:105696. https://doi.org/10.1016/j.optlastec.2019.105696

16. Michler M, Hollmann P, Zenker R, Buchwalder A (2021) Investigation of pore reduction in hybrid joints of conventionally and additively manufactured AlSi10Mg using electron beam welding. Adv Engg Mate 23:2001325. https://doi.org/10.1002/adem.202001325

17. Wits WW, Becker JJ (2015) Laser beam welding of titanium additive manufactured parts. Proced Cirp 28:70–75. https://doi.org/10.1016/j.procir.2015.04.013

18. Chen N et al (2022) Effect of ambient pressure on laser welding of AlSi10Mg fabricated by selected laser melting. Mat Des 215:0264–1275. https://doi.org/10.1016/j.matdes.2022.110427

19. Biffi CA, Fiocchi J, Tuissi A (2019) Laser weldability of AlSi10Mg alloy produced by selective laser melting: microstructure and mechanical behavior. J Mater Eng Perform 28:6714–6719. https://doi.org/10.1007/s11665-019-04402-7

20. Iordachescu D, Blasco M, Lopez R, Cuesta A, Iordachescu M, Ocaña JL (n.d.) Development of robotized laser welding applications for joining thin sheets

21. "Robots and Laser Welding, the Perfect Fit https://www.automate.org/industry-insights/robots-and-laser-welding-the." [Online]. Available: https://www.automate.org/industry-insights/robots-and-laser-welding

22. Hadadzadeh A, Amirkhiz B, Shakerin S, Kelly J, Li J, Mohammadi M (2020) Microstructural investigation and mechanical behavior of a two-material component fabricated through selective laser melting of AlSi10Mg on an Al-Cu-Ni-Fe-Mg cast alloy substrate. Addit Manuf 31. https://doi.org/10.1016/j.addma.2019.100937

23. Salmi A, Atzeni E, Iuliano L, Galati M (2017) Experimental analysis of residual stresses on AlSi10Mg parts produced by means of selective laser melting (SLM). Procedia CIRP 62:458–463. https://doi.org/10.1016/j.procir.2016.06.030

24. Xiong ZH, Liu SL, Li SF, Shi Y, Yang YF, Misra RDK (2019) Role of melt pool boundary condition in determining the mechanical properties of selective laser melting AlSi10Mg alloy. Mater Sci Eng A 740–741:148–156. https://doi.org/10.1016/j.msea.2018.10.083

25. Asghar G, Peng L, Fu P, Yuan L, Liu Y (2020) Role of Mg 2 Si precipitates size in determining the ductility of A357 cast alloy. Mater Des 186:108280. https://doi.org/10.1016/j.matdes.2019.108280

26. Marola S, Bosia S, Veltro A, Fiore G, Manfredi D, Lombardi M, Amato G, Baricco M, Battezzati L (2021) Residual stresses in additively manufactured AlSi10Mg: Raman spectroscopy and X-ray diffraction analysis. Mater Des 202:109550. https://doi.org/10.1016/j.matdes.2021.109550

27. Fulcher BA, Leigh DK, Watt TJ (2014) Comparison of AlSi10Mg and Al 6061 processed through DMLS. 25th Annu Int Solid Free Fabr Symp and #65533. An Addit Manuf Conf SFF 2014:404–419

28. Vander Voort, George F (1984) Metallography: principles & practice, ASM International. New York : McGraw-Hill. https://doi.org/10.31399/asm.tb.mpp.9781627082600

29. Hadadzadeh A (2019) Babak Shalchi Amirkhiz, Mohsen Mohammadi, Contribution of Mg2Si precipitates to the strength of direct metal laser sintered AlSi10Mg. Mater Sci Eng, A 739:295–300. https://doi.org/10.1016/j.msea.2018.10.055